https://doi.org/10.1016/j.jpowsour.2021.230340

Alleviation on battery thermal runaway propagation: Effects of oxygen level and dilution gas

Jingwen Weng[1], Dongxu Ouyang[1], Yanhui Liu[2], Mingyi Chen[4], Yaping Li[3], Xinyan Huang[2,*], Jian Wang[1,*]

[1] *State Key Laboratory of Fire Science, University of Science and Technology of China, Hefei, China*

[2] *Research Centre for Fire Safety Engineering, Department of Building Services Engineering, Hong Kong Polytechnic University, Kowloon, Hong Kong*

[3] *USTC Center for Micro and Nanoscale Research and Fabrication, University of Science and Technology of China, Hefei, China*

[4] *School of Environment and Safety Engineering, University of Jiangsu, Zhenjiang, China*

**corresponding to wangj@ustc.edu.cn (J. Wang); xy.huang@polyu.edu.hk (X. Huang)*

Abstract

The thermal safety issue of the lithium-ion batteries (LIBs) is a key challenge in new energy storage systems, and novel protection strategies for battery fire and explosions are urgently needed. In this experimental study, the thermal runaway and fire behaviors of cylindrical LIBs are explored in the ambient oxygen concentration from 12% to 21% with the dilution gas of nitrogen and argon. The X-ray CT imaging and energy-dispersive spectrometry are used to assist the micro morphology analysis. The results show that the thermal runaway time interval (between Layers 1 and 2) increases from 136 s (21% O_2) to 196 s (12% O_2), indicating the thermal-runaway propagation rate is reduced by 44%. Moreover, the mass loss and flaming combustion are both weakened when reducing the oxygen concentration. Whereas, the oxygen concentration has little influence on the maximum cell temperature during thermal runaway (600-800 ℃). Comparison between nitrogen and argon dilutions shows a similar effectiveness in alleviating thermal runaway propagation, so the nitrogen dilution is more cost effective. The X-ray CT imaging and energy-dispersive spectrometry show less molten drops and much less fluorine in the burnt cell at a higher oxygen level. This study provides new references for improving the safer transport and storage of battery modules and fire protection strategies.

Keywords: *Lithium-ion battery safety; thermal runaway propagation; inert gas dilution; oxygen concentration*

Abbreviations

LIB	lithium-ion battery	T	Temperature
PCM	phase change material	V	Volt
N_2	nitrogen	A	Ampere
O_2	oxygen	A h	Ampere-hour
CO_2	carbon dioxide	Pa	Pascal
Ar	argon	atm	atmosphere
CT	computer tomography	t	time
SEM	scanning electron microscopy	DAQ	data acquisition
EDS	energy-dispersive spectrometry	CC	constant current
IR	infrared	SOC	state of charge
SI	supplementary information		

Nomenclature

n	reaction order	S_L	layer-based propagation speed
N	number of cells	$\dot{q}_f$	flame heating
m	mass of the cell	$\dot{q}_b$	heat conduction
Δm	mass loss	$\dot{q}_r$	heat release f
s	propagation speed	$\dot{q}_c$	environmental cooling
f	mass function	m_b	mass of Layer-2 cells
Z	pre-exponential factor	m_0	mass of battery cells excluding the heater
E	activation energy	c_b	specific heat capacity
R	universal gas constant	T_{TR}	onset temperature of thermal runaway
Subscripts		T_a	initial battery/ambient temperature
T_{max}	maximum temperature	h_f	overall coefficient of flame heating
$\overline{t_{L1}}$	thermal-runaway time	T_f	flame temperature
t_i	thermal runaway onset time	$\overline{\Delta t}$	time interval
T_{Ki}	temperature	Δm	mass loss

1. Introduction

Lithium-ion batteries (LIBs) have been widely used in electric vehicles [1, 2], portable devices [3] and other fields due to their high energy density [4, 5] and long-cycle lifespan [6-8] but risks of their thermal hazards rise simultaneously [9, 10]. With enormous fire and explosion accidents linked with LIB thermal runaway [11-13], their fire safety issue has been brought to spotlights [14-18]. The thermal runaway of a single LIB cell is a complex and violent process [19] with fire and sometimes even explosions [20, 21], during which a large amount of heat will be released coupled with hot aerosols and flammable gases ejected at a high speed [22, 23]. With this effect, the thermal runaway propagation will be aggravated and exhibit a domino-like propagation [24-26], resulting tremendous disasters for the battery modules and the whole energy storage system [27]. Besides, the injection gases and smokes from the overheated battery and flame are highly toxic [28, 29], which harms humankind's health and pollutes the air. Therefore, it is critical to prevent or limit the flame during the battery thermal runaway to alleviate fire hazard and mitigate environmental pollution [30, 31].

Faced with this challenge, a number of researchers have devoted to develop new strategies to prevent or alleviate battery thermal runaway propagation and battry fire [32-34]. For example, Wilke et al. [35] proposed that the use of phase change materials (PCMs) was a promising approach to prevent thermal runaway propagation. Li et al. [36] assembled aluminum plates into battery modules as heat sinks to mitigate thermal runaway propagation. In our previous study, we also proposed a new module design by coupling flame-retarded PCMs with arogel felt to alleviate thermal runaway propagation [37].

The abovementioned approaches indeed obtained some remarkable positive effects [38]. However, most of these strategies inevitably reduced the energy density by implementing additional devices in the battery modules. From this perspective, it is imperative to develop novel strategies to alleviate the battery thermal runaway without reducing the energy density. Inspired by Said et al. and S.I. Stoliarov et al's studies [39-41], inert gas dilution has been regarded a promising strategy to alleviate battery fire. In the fire research, inert gas dilution is a commonly used method to extinguish the fire and suppress explosion that can lower the flame temperature and the flammability limit [42-44]. Nitrogen (N_2), carbon dioxide (CO_2) and argon (Ar) are extensively employed to fight conventional fires [45, 46]. Introducing an excessive amount of these inert gases can lower the oxygen concentration to smother the flame [47, 48]. Usually, flame can hardly exist below 12% oxygen concentration for common hydrogen fuel gases [42, 49]. Moreover, inert gases dilution is effective to reduce the concentration of toxic gas emissions, which has been confirmed by several studies [43, 44].

Nevertheless, the scientific knowledge of inert gas dilution on battery fire is still limited, and the effectiveness has not been fully understood. For example, the influence of N_2 dilution and oxygen concentration had not been fully addressed in previous work. Given to the complexity of the chemical reactions in battery fire [50, 51], the research gap undoubtedly barriers the further application of the inert gas dilution strategy in the battery safety research. Besides, the selection of dilution gas is also worth further investigation. Therefore, a systematical investigation on the viability and suitability of

inert gas dilution on battery fire extinction is urgently needed to meet the ever-increasing demands of thermally safer and more reliable battery systems.

In this study, a series of experiments is conducted on cylindrical Li-ion battery packs to investigate the alleviation effects of inert dilution gas on battery thermal runaway propagation. Given the fact that it is extremely difficult to create an environment free of oxygen in real application and usually the flame can hardly exist below 12% oxygen concentration for common hydrogen fuel gases [42, 49], the gas dilution environment is set with the oxygen concentration from 21% to 12%. Second, two different dilution gases (nitrogen and argon) are experimented to compare their effects on inhibiting the battery fire and thermal runaway propagation. It should be noted that a high level of CO_2 can cause hypercarbia, thus using dilution gases of N_2 and Ar is safer in fire suppression. Third, multiple methods are applied to provide new references on the investigated issue of this work. The X-ray computer tomography (CT) imaging and energy-dispersive spectrometry (EDS) are used to compare the internal structure changes and micro morphology of the fresh and burnt cells in different configurations. Besides, infrared (IR) images coupled with point-thermocouple temperature data are analyzed to quantify the domino-like thermal runaway propagation characteristics. Finally, the recommendations of oxygen level and dilution gases are provided to improve the battery fire safety in storage and transportation.

2. Experiment

2.1 Battery samples

Commercial 18650 lithium-ion batteries (INR18650-20R, Samsung SDI Co., Ltd) with the nominal capacity of 2.0 Ah and nominal voltage of 3.6 V were used in this work. Before the test, the original energy stored in the batteries was released by discharging in a constant current (CC) mode with proper C-rate (C-rate is the measurement of the charge and discharge current with respect to its nominal capacity) until the voltage decreased to 2.75 V, and then the batteries were charged to 75% state of charge (SOC). After the SOC calibration process, the batteries were maintained for 24 h to ensure their stability. The same batch of batteries was used in this study to minimize the influence of the non-uniformity of cells.

2.2 Experimental apparatus

Fig. 1a illustrates the experimental platform used in this work. Experiments were carried out in a combustion chamber, whose dimension was 3 m in length, 2 m in width, and 2 m in height. This chamber can provide a relatively-stable environment by controlling the inlet and outlet gas flow dynamically. Inside the chamber, the battery module was placed on a steel supporting mesh. As shown in Fig. 1b, the supporting mesh was placed on a lifting platform covered by a fire-proof board, so the height of the battery module could be adjusted. A cylindrical heater with the same size as the 18650 LIB cell (i.e., a dummy of 18-mm diameter and 65-mm height) and a constant power of 300 W power was applied to simulate the overheated battery to trigger the thermal runaway propagation to adjacent cells.

The K-type thermocouple with the diameter of 1 mm was attached on the center surface of each cell to measure its surface temperature. In addition, four thermocouples were placed above the battery module align with its geometric center like a tree to monitor the temperature of ejected gases and jet flame. All temperature data were recorded by the data acquisition equipment (NI cDAQ-9174). During the test, a video camera (SONY XPS160) and an infrared imager (FLIR T650sc2.1) were used to monitor the fire phenomena and thermal runaway propagation.

Furthermore, the structural characteristics of the fresh and burnt cells were analyzed by X-ray computed tomography (CT) using an X-ray Microscopy (ZEISS Xradia 520 Versa). In addition, the Energy-dispersive spectrometry coupled with field emission scanning electron microscopy (SEM-EDS) characterization [52] was performed using a Hitachi SU 8220 FESEM equipped with an Oxford X-Max SDD system (Oxford Aztec X-Max80).

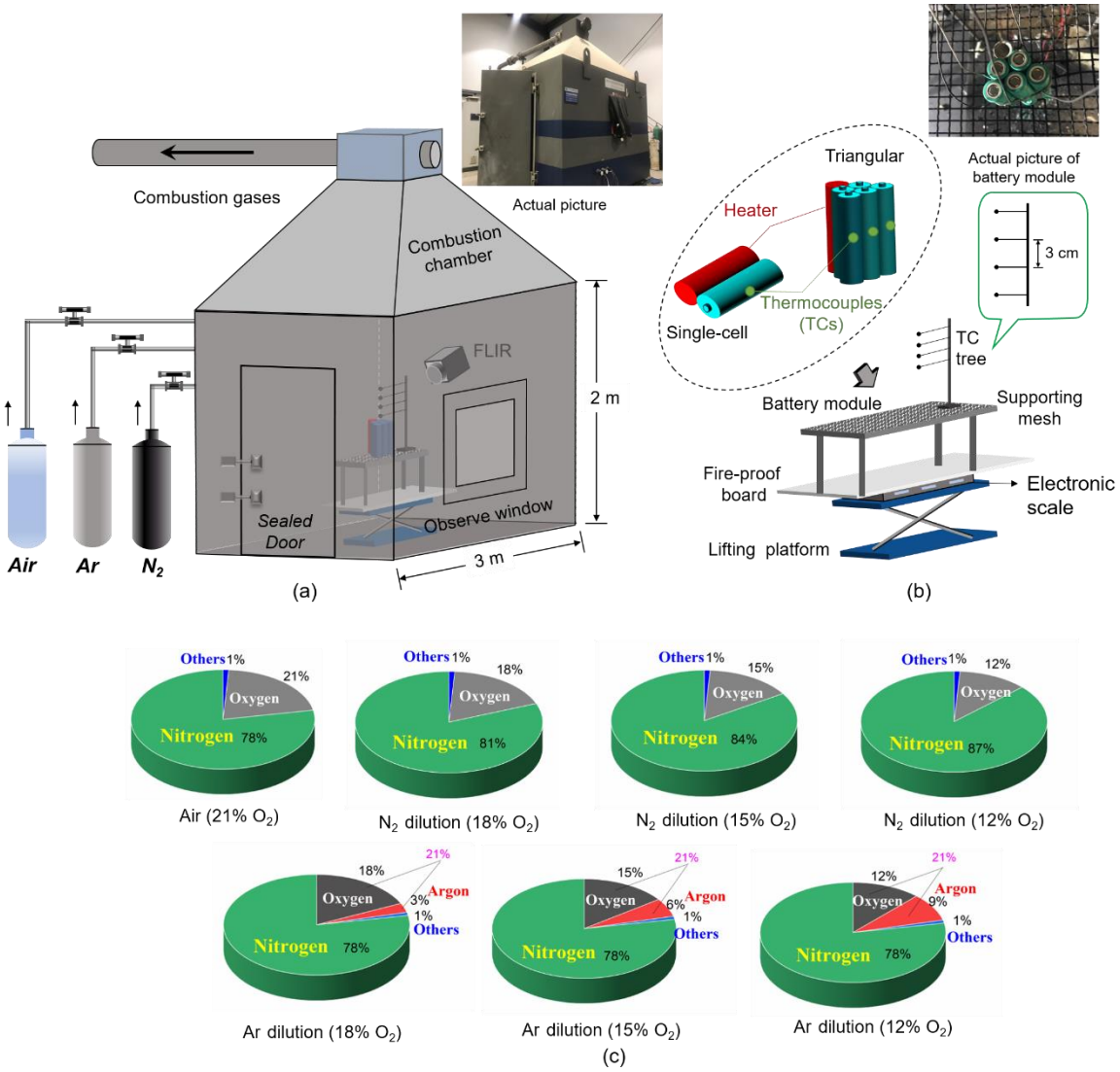

Fig. 1. Schematic diagram for experimental setup: (a) thermal runaway platfor; (b) battery module arrangement; and (c) atmospheric composition under different oxygen concentrations without and with N_2 or Ar dilution.

2.3 Experimental design and procedure

In this work, all experiments were conducted at an ambient pressure of 90 ± 2 kPa (or 0.9 atm), the purpose of which was to ensure airtightness of the test chamber. Given the atmospheric pressure, the reference tests were also implemented at the normal ambient pressure (100.8 kPa). The comparison of thermal runaway phenomena between 100.8 kPa and 90 kPa is illustrated in Fig. S2 and discussed in the Supplementary Information (SI). All tests were conducted under ambient temperature of 15±2 ºC. During the experiments, three key parameters were controlled:

(I) Battery arrangements. As depicted in Fig. 1b, two types of battery arrangements were examined in this work, i.e., a single-cell module and a triangular module. For the single-cell module, both the electrical heater and the battery cell were horizontally placed on the supporting mesh, where an iron wire was used to ensure tight contact between the heater and cell. In terms of the triangular module, five cells and the heater were arranged in a triangular shape, and the module was vertically fixed on the supporting mesh.

(II) Type of dilution gases. The inert gases nitrogen (N_2) and argon (Ar) with high purity (purity > 99.999 %) were chosen. Their physical properties, along with a comparison with standard air and oxygen under the normal condition, are listed in Table 1.

(III) Oxygen concentration. Four oxygen mole fraction (or concentration) of 21%, 18%, 15%, and 12% were selected for experiments. The atmospheric compositions inside the pressure chamber under different oxygen concentrations are illustrated in Fig. 1c.

Table 1. Physical properties of air, N_2, and Ar at the normal condition (1 atm and 15 ℃).

Gas	Toxic	Inert gas*	Molecular mass (g/mol)	Relative density (kg/m^3)
Air	No	No	29	1
O_2	No	No	32	1.10
N_2	No	Yes	28	0.97
Ar	No	Yes	40	1.66

* those do not undergo chemical reactions under general conditions. In a broad sense, nitrogen is considered an inert gas.

Before the experiments, the combustion chamber pressure was maintained stable at 90 kPa. Then, the automatic gas control system was opened to allow the dilution gas to enter the combustion chamber until the oxygen content dropped to the desired value. The oxygen concentration would be stable for at least five minutes before the battery test started. The detailed controlled patterns and the instrument error of the combustion chamber were analyzed in the SI (Fig. S1 in the SI). The gases produced during the experimental process were extracted using an exhaust fan, and the environment of the chamber would be refreshed with air at the end of each test.

3. Results and discussion

3.1 Effects of battery arrangement and basic theory

As the reference group, the temperature variations of single-cell and the triangular module at the normal air composition (21% O_2) at 90 kPa are summarized in Fig. 2, where the photographs of some typical moments are presented.

***Single cell*:** In general, the thermal runaway behaviors of a single cell follow similar processes of our previous studies [53]. According to the temperature curve in Fig. 2a, the thermal runaway behavior of a single cell can be divided into three phases, i.e., (I) the heating, (II) the gassing, and (III) the thermal runaway. At the first heating stage, under continuous heating by the heater, the cell temperature increases steadily. With the battery temperature rising, the exothermic electrochemical reactions inside the battery cell are triggered, producing a lot of electrolyte vapors and flammable gases inside the cell. As a consequence, the internal pressure increases violently. At the second gassing stage, the safety valve fails to withstand the high pressure inside the cell, so the venting occurs. The flammable gases as well as electrolyte vapor rushes out of the battery and starts to react with the air. The third thermal-runaway stage is marked by the ignition of flame and flame ejections from the battery. As shown in Fig. 2a, the violent flame ejections can be observed, accompanied by the sharp temperature increase of the battery cell (exceeding 690 °C at approximately 22.67 °C/s in this test) and a great amount of smoke releasing.

***Triangular module*:** Normally, multiple cells can be arranged into specific shapes for a module to meet the required voltage and energy capacity, which poses higher fire risks. Fig. 2b describes the thermal runaway behaviors of a triangular module, where all cells reached thermal runaway within 420 s. In this test, the measured maximum temperatures (T_{max}s) of several cells can exceed 750 °C, which is higher than 694 °C found in the single-cell test. This confirms that higher fire-propagation risks in the applications of multi-cell battery packs/modules [54].

As found in many previous studies [32, 40], a domino-like propagation of thermal runaway is expected in the multi-cell battery modules. In this triangular module, a domino-like cascading failure is also observed. In order to further explore the domino-like propagation of thermal runaway within the triangular battery module, the back-view camera images and side-view infrared images are displayed in Fig. 2c. At the heating stage, although little change can be seen from the camera, the heat transfer from layer to layer is clearly seen from the infrared images. For example, surfaces of battery Cells 1 and 2 in Layer-1 are soon heated up due to a close contact with the heater, while the Layer-2 Cells 3, 4, and 5 remain a much lower temperature.

At about 279 s, the thermal runaway of Layer-1 is triggered, followed by the flaming ignition, violent ejection, and continuous jet flame. Under the heating effect of flame, the air surrounding the battery cell is soon heated up, as shown by the gas-phase color change in the infrared images. The sharp temperature increases of the Cells 3, 4, and 5 are also found in Fig. 2c, indicating simultaneous fast heating in the battery cell along with the jet flame. After another 142 s, the battery temperature of Layer-2 continues to heat up, being exposed to the jet flame by cells in Layer-1. This confirms that the battery flame plays a dominant role in the thermal-runaway propagation over the battery module compared to the conductive heat transfer among cells, which are in accordance with the references [26, 51]. The

occurrence of thermal runaway way of last cell (i.e., Cell 5) at about 460 s marks the total failure of the whole module.

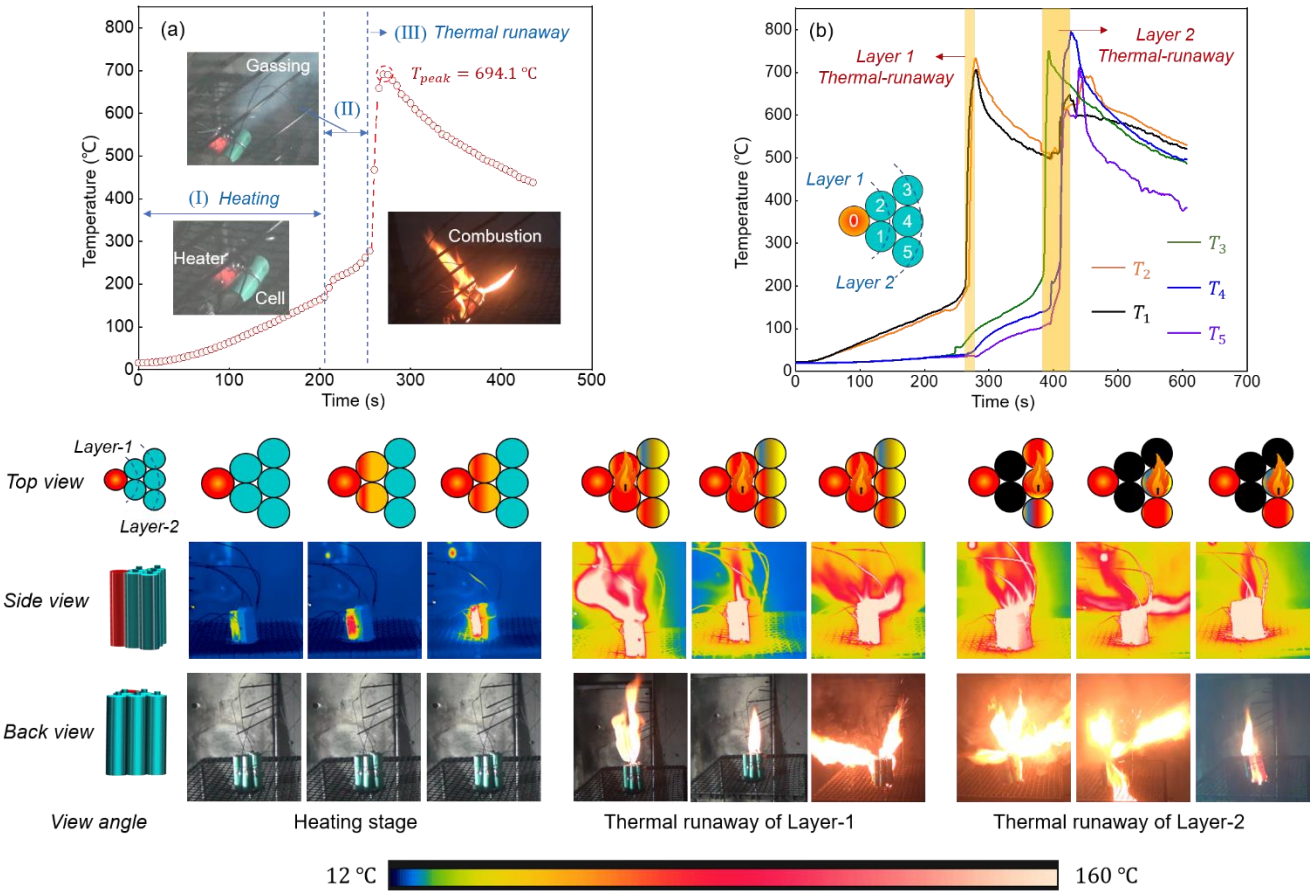

Fig. 2. Battery temperature curves: (a) single-cell and (b) the triangular module (5 cells) at 21% O_2 (i.e. air); and (c) schematics, infrared images, and photographs of the domino effect in the battery module.

According to the theory of *Frank-Kamenetskii*, the battery module/pack consisting of a larger number of cells has a greater tendency of thermal runaway with heat accumulation and poor environmental cooling [55]. The internal thermal runway will propagate from cell to cell and from layer to layer like a domino chain reaction [56]. As found in our previous study [57], the total heat release in the battery module increase with the battery numbers. Hence, to alleviate the domino-like thermal-runaway propagation among layers in the battery module, weakening the battery jet flame is a promising methodology, and reducing the environmental oxygen concentration is an effective method to suppress and even extinguish the flame.

3.2 Effects of oxygen concentration

To mitigate the battery jet flame, the inert gas dilution is an effective measure by lowering the environmental oxygen concentration. Thus, experiments were conducted in the ambient of different oxygen levels with N_2 dilution to the impact on the rate of thermal-runaway propagation and jet flame.

3.2.1 Thermal runaway propagation behavior

Fig. 3 compares the surface temperature of all five battery cells at the oxygen concentration decreasing from 21% to 12%. For conventional hydrogen fuels [42, 49], the limiting oxygen concentration (LOC) of their flame is usually above 12%, so that they cannot maintain a flame at a low oxygen concentration of 12%. However, for the battery thermal runaway, reducing the oxygen concentration from 21% to 12% is not sufficient to eliminate the battery flame. There are a few reasons. First, during thermal runaway, the battery internal temperature and the ejected fuel gases can exceed 800 ℃, so that these preheated fuel gases can extend the LOC and fuel flammability. In addition, highly active lithium particles exist in the fuel jet that can induce strong exothermic reactions, even if the oxygen concentration is low.

Although the battery jet flame cannot be fully extinguished, reducing the oxygen concentration indeed slows down the propagation of battery thermal runaway and flame. To quantify the effectiveness of fire mitigation, the propagation time ($\overline{\Delta t}$) should be first calculated. Given to the inconsistency of the onset time caused by the individual differences of each cell in the battery module, the average time is defined to support further discussion, denoted as

$$\overline{t_L} = (\sum_{i=1}^{n} t_i)/n \tag{1}$$

where t_i is the thermal runaway onset time of cell *i* (*i*= 1, 2, 3, 4, and 5), and *n* is the cell number of that layer (*n* = 2 for Layer 1 and n = 3 for Layer 2). Then, the characteristic thermal-runaway time of $\overline{t_{L1}}$ and $\overline{t_{L2}}$ for Layer-1 and Layer-2 can be calculated as

$$\overline{t_{L1}} = (t_1 + t_2)/2 \tag{2}$$

$$\overline{t_{L2}} = (t_3 + t_4 + t_5)/3 \tag{3}$$

Therefore, the time interval between two layers (Δt) is

$$\overline{\Delta t} = \overline{t_{L1}} - \overline{t_{L2}} \tag{4}$$

Fig. 3 shows three phases in the thermal-runaway propagation. Phase I refers to the heating stage before thermal runaway, where the heat conducted from the heater to Layer 1 (major) and Layer 2 (minor). From the temperature curves and infrared images, the heater shows a little heating effect on Layer 2. A clear temperature rise of Layer 2 is only observed after the thermal runaway of Layer 1, which is the beginning of Phase II. During this phase, the temperature rise of Layer-2 is mainly attributed to two heat sources, i.e., the heat conduction from the hot battery and the jet flame.

When the oxygen concentration is reduced from 21% to 12%, the jet flame of Layer-1 batteries becomes weak; thus, the convective and radiant heat transfer from the flame to Layer-2 batteries is reduced. Consequently, the thermal-runaway time for Layer 2 is delayed. As illustrated in Fig. 3, the time interval (between Layers 1 and 2) increases from 136 s (21% O_2) to 196 s (12% O_2). In other words,

the rate of thermal-runaway propagation is reduced by 44%. Moreover, due to less heat transferred from flaming combustion, the temperature rise rate of the Layer-2 cells is reduced. For example, the heating rates of Cell 3 are 0.53 ºC/s at 21% O_2, 0.50 ºC /s at 18% O_2, 0.49 ºC /s at 15% O_2, and 0.43 ºC /s at 12% O_2 below the onset temperature of thermal runaway (about 200 ºC). Finally, after the thermal runaway of all batteries, the cooling process by the environment dominates Phase III. Note that the peak temperature of the battery cell (750-800 ºC) during the thermal runaway is less sensitive to the oxygen concentration, because it is mainly determined by the internal electrochemical reactions rather than the external heat transfer.

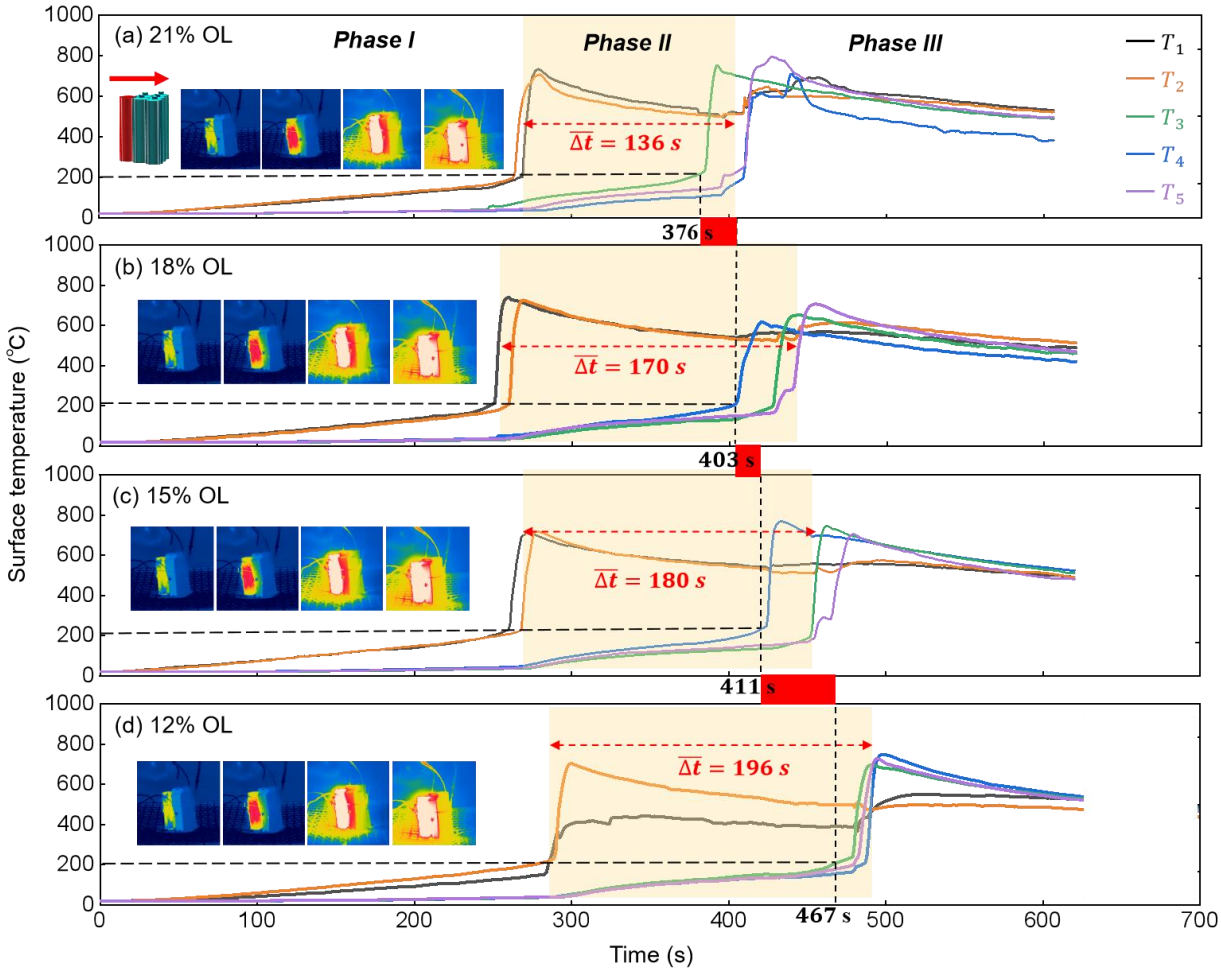

Fig. 3. Temperature variations of the battery modules under different oxygen concentrations.

3.2.2 Mass loss of battery cells

Fig. 4a presents the mass-loss evolution of the triangular module during the thermal runaway process. In general, there are three semi-platforms and two sharp drops in the mass-loss curves, regardless of oxygen level. The two mass drops correspond to the thermal runaway of Layer 1 and Layer 2. Referring to the temperature evolution in Fig. 3, although battery temperature is rising in phase I, there is almost no mass loss before the ejection of battery materials. At the beginning of Phase II comes the first sharp mass loss ($\overline{\Delta m_1}$), which is due to the violent ejection of internal gases. It should be noted

some points showing sudden mass gain are caused by the bounce or the impact of the violent ejection on the electronic balance. By comparison, the $\overline{\Delta m_1}$ is most insensitive to the ambient oxygen level, because the ambient oxygen is not involved in the internal reactions that trigger the thermal runaway.

Afterwards, the mass decreases slowly and steadily in Phase II, and the jet flame becomes stable until the end of the Layer-1 thermal runaway. The mass loss during Phase II (or the amount of fuel to feed the flame) is smaller than the step mass loss of $\overline{\Delta m_1}$, so that the majority of ejected gases may not be burnt in flame. More importantly, during Phase II, larger mass loss are observed at a higher oxygen concentration. It is because the flame is more intense and violent at a higher oxygen concentration, which can generate a larger heat flux to accelerate the propagation of thermal runaway.

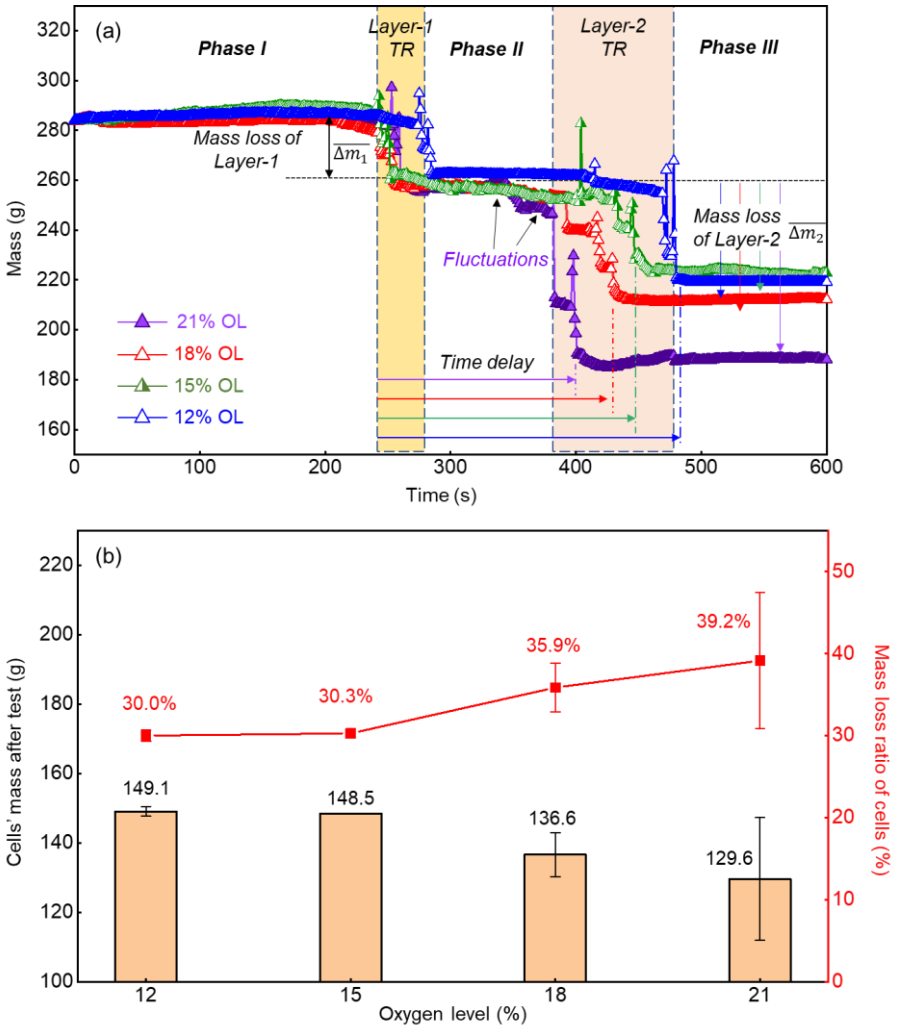

Fig. 4. Mass loss of battery modules experimented at different oxygen concentrations: (a) mass loss curves; (b) total mass change and corresponding ratio.

Unlike the first mass drop of Layer 1 that is insensitive to O_2, the second sharp mass drop before phase III ($\overline{\Delta m_2}$) burnt in the 21% O_2 is the largest, indicating more battery internal materials ejected during the thermal runaway of Layer 2. It is mainly because the stronger flame heat flux causes a more violent thermal runaway and ejection of Layer-2 cells. Fig. 4b further summarizes the total mass change

for the battery modules vs. the oxygen concentration. The initial mass of the battery module is approximately 284.0 g, including five battery cells (about 42.6 g per cell) and an 18650 cell-like heater (about 70.9 g). For the battery residues, the masses are 129.6 g, 136.6 g, 148.5 g, 149.1 g, and at 21%, 18%, 15%, and 12% O_2, respectively. The corresponding mass loss ratios of the cells excluding the heater, $(\overline{\Delta m_1} + \overline{\Delta m_2})/ m_0$, m_0 is the mass excluding the heater (213.1 g), are 39.2%, 35.9%, 30.3%, and 30.0%, respectively. This further suggests that reducing the oxygen concentration not only directly suppresses the flame, but also indirectly weakens the thermal-runaway processes of the batteries.

3.2.3 Flame characteristics

To further quantify the characteristics of the battery jet flame, Fig. 5a shows the temperature data measured by the thermocouple tree at different heights (T_{K1}, T_{K2}, T_{K3}, and T_{K4}) above the battery module at different oxygen concentrations. First, there is an obvious temperature drop with decreasing O_2, which is most apparent for T_{K1} (i.e., the lowest point and closest to the module). For example, the peak temperature for T_{K1} in 21% O_2 is 886 ℃, which decreases by 75% to 217 ℃ in 12% O_2. Whereas for T_{K4} (i.e., the highest point and furthest away from the module), it drops by 36% from 554 ℃ (21% O_2) to 352 ℃ (12% O_2), which indicates the flame may not reach T_{K4}.

Note that the jet flame may not in direct contact with the thermocouple beads, so the measured temperature is more a reference temperature of that height rather than the flame temperature. For the same reason, the number of temperature peaks varies in different cases and even the repeating tests. For example, at 21% O_2, there is only one peak temperature, and the high-temperature stage is continuous, because the hot jet and flame are taller and more intense that can continuously hit all thermocouple beads. In other low-O_2 cases, the peak temperatures are lower and appear more than once, because the flame is weaker and less continuous.

Fig. 5b shows a group of experiments with flame pattern (photos) and flame durations (pie chart) at different oxygen concentrations (also see Videos S1-S3). With the decrease in oxygen concentration, the duration of the flame is rapidly reduced proportionally during the thermal runaway process, that is, from 193 s (93% of 207 s) at 21% O_2 to 41 s (18% of 224 s) at 12% O_2. The total duration in the pie chart is counted from the beginning of the first occurrence of the flame, excluding the initial heating time. The flame duration refers to the appearance of flame among the total duration. With 21% and 18 % oxygen concentrations, the yellow flames are larger and brighter, suggesting a lot of soot formation and radiation. However, lowering the oxygen concentration to 15% and 12 %, the flame is weaker, smaller, and less intense, due to the slower flame chemical reactions and lower flame temperature (i.e., the suffocation/smothering effect). Nevertheless, the yellow flame changes into red color, due to the oxidation of metals in flame, so it is different from other hydrocarbon fuels that have a blue flame in low oxygen concentration [58].

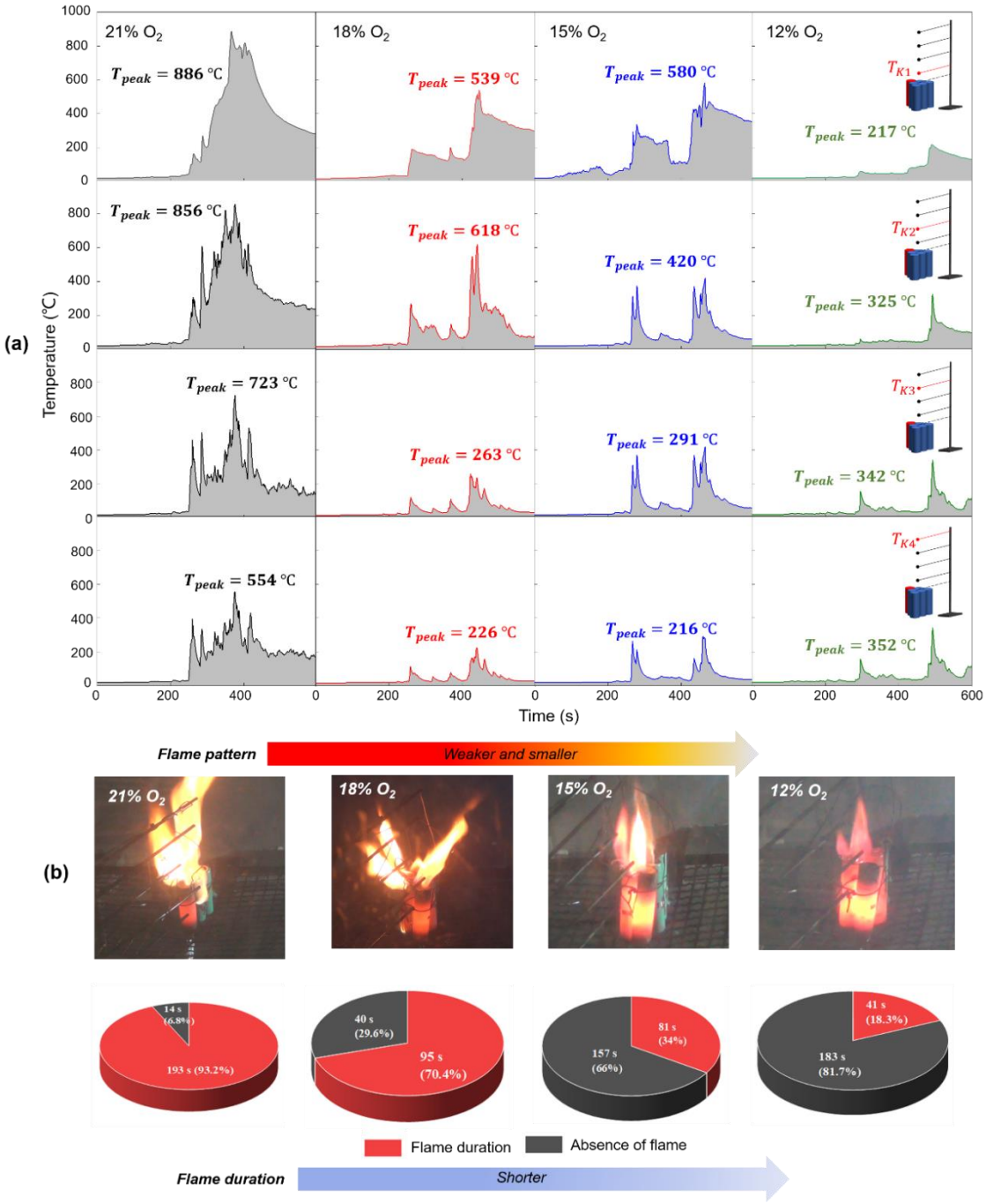

Fig. 5. (a) Temperature data measure by the thermocouples at different heights above the battery module in different oxygen concentrations, and (b) flame duration and change of flame pattern with changing oxygen concentration.

3.2.4 Rate of thermal runaway

As discussed above, the battery jet flame has a significant impact on thermal runaway propagation from Layer-1 cells to Layer-2 cells. To characterize the thermal runaway propagation on the battery module, a layer-based propagation speed ($S_L, layer/min$) can be defined as

$$S_L = N_L / \overline{\Delta t} \tag{5}$$

where N_L is the number of propagation layers, and $\overline{\Delta t}$ is the mean propagation time. In this triangular module, $n_L = 1$ and $\overline{\Delta t} = \overline{\Delta t_{12}}$. In this way, Eq. (5) can be expressed as

$$S_L = 1/\overline{\Delta t_{12}} = 1/(\overline{t_{L2}} - \overline{t_{L1}}) \tag{6}$$

The layer-based propagation speed S_L varying with the oxygen concentration is summarized in Fig. 6, where the error bar shows the uncertainties among repeating tests. It is observed that the value of S_L decreases with the reducing oxygen concentration. At 21% O_2, S_L is 0.43 layer/min, while the propagation rate decreases by 28% to 0.31 layer/min at 12% O_2.

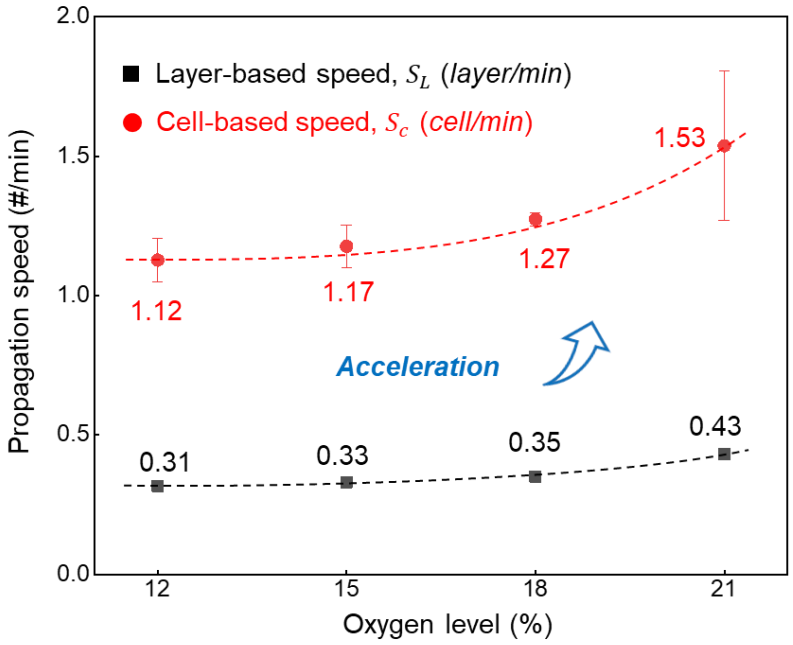

Fig. 6. Thermal-runaway propagation speed varying with the ambient oxygen concentration.

The sufficient condition of the cascading failure propagation from Layer 1 to Layer 2 is that cells in Layer-2 can be heated to the onset temperature of thermal runaway. Similar to the flame spread, the propagation rate of thermal runaway is controlled by the heat transfer between layers (driven force) and the thermal inertia of cell (resistance). To qualitatively analyze the effect of oxygen concentration on thermal runaway propagation, a simplified heat transfer model is performed where the battery layer is assumed as uniform internally. Therefore, the propagation speed could be given by

$$\begin{aligned} S_L &= \frac{\text{net heating effect}}{\text{minimum energy for thermal runaway}} \\ &\approx \frac{\dot{q}_f + \dot{q}_b + \dot{q}_r - \dot{q}_c}{m_b c_b (T_{TR} - T_a)} \qquad [\text{layer/min}] \end{aligned} \tag{7}$$

where $\dot{q}_f$ is the flame heating on Layer-2 cells (W), which includes convection and radiation; $\dot{q}_b$ is the heat conduction from Layer-1 cells to Layer-2 cells through the shells (W); $\dot{q}_r$ is the heat release from exothermic reaction inside Layer-2 cells before the thermal runaway (W); $\dot{q}_c$ stands for the

environmental cooling (W); m_b is the mass of Layer-2 cells (g); c_b is the specific heat capacity (J/g-k); $T_{TR} \approx 200$ ℃ is the onset temperature of thermal runaway (see Fig. 3); and $T_a \approx 15$ ℃ is the initial battery/ambient temperature (℃). Apparently, except for $\dot{q}_f$ and $\dot{q}_r$, all other parameters are independent of the ambient oxygen.

The flame heating ($\dot{q}_f$) can be described by the heat transfer between the flame and battery cell as

$$\dot{q}_f = h_f A\left(T_f - T_{TR}\right) \tag{8}$$

where h_f is the overall coefficient of flame heating (W/m^2-K); A is the effective cell surface area heated by flame; and T_f is the flame temperature (K). According to Fig. 5, the measured temperature increases with the oxygen concentration, so that a higher oxygen level can lead to a higher $\dot{q}_f$.

For the heat generation inside cells before the thermal runaway, $\dot{q}_r$ could be estimated by the following equation:

$$\dot{q}_r = \sum \Delta H f^n Z \exp(-E/RT) \tag{9}$$

where ΔH is the heat of reactions; f is the mass function that depends on the concentration of reactants; n is the reaction order; Z is pre-exponential factor; E is the activation energy; R is the universal gas constant; and T is battery temperature. It is possible that some oxygen leaks into the battery cells to cause exothermic oxidation before the onset of thermal runaway. The effect of oxygen concentration on $\dot{q}_r$ has been studied by Fu et al. [59], where the lower oxygen concentration can lower $\dot{q}_r$ by weakening the thermal decomposition reactions inside the cells. Therefore, decreasing the oxygen concentration through extra inert gas dilution can reduce the value of both $\dot{q}_f$ and $\dot{q}_r$. Then the numerator in Eq. (3) decreases, resulting in the reduction of layer-based propagation speed. Except for slowing the thermal runaway propagation, diluting the oxygen concentration can significantly decrease the fire hazards after thermal runaway of the entire module.

To generalize the test results for other different modules, the cell-based propagation speed (S_c, cell/min) and total mass loss are also employed to quantify such effects in the cell level. The cell-based propagation speed (S_c, cell/min) refers to an average failure propagation rate of the battery module as

$$S_c = \frac{N-1}{t_n - t_1} \quad [\#/\text{min}] \tag{10}$$

where N is the number of cells; t_n is thermal-runaway time of the last cell while t_1 represents the thermal-runaway time of the first cell. As shown in Fig. 6, a higher oxygen concentration can significantly accelerate the propagation speed. Specifically, the thermal-runaway speed is 1.53 cell/min with the module at 21% O_2, which is 1.36 times as fast as that of the module at 12% O_2. Thus, for the large battery system, diluting the oxygen concentration can slow down the thermal-runaway propagation and minimize the fire hazards.

3.3 Effects of dilution gases

According to the previous subsection, it is an effective approach to delay the domino effect by filling the chamber with inert gas. An alternative inert gas, Ar, is investigated in this section. Fig. 7a and Fig. 7b presents the fire behaviors of battery modules in argon and nitrogen dilutions with 15 % oxygen concentration. In general, the stages of fire behaviors in both argon and nitrogen gas dilution environment are similar to that in the air.

Similar to the N_2 dilution mentioned in the previous section, the flaming time is reduced, and the jet flame becomes weaker, smaller, and less continuous. Due to the incomplete combustion in the oxygen-lean environment, the ejected electrolyte will be more difficult to ignite but leftover on the cell. Therefore, the re- phenomenon can be observed several times once the local premixed fuel jet reaches the flammability limit.

Fig. 7c further compares $\overline{t_{L1}}$ and $\overline{t_{L2}}$ between nitrogen and argon dilutions for different oxygen concentrations. Objectively, no distinct difference can be observed between two dilution gases, and both nitrogen and argon dilutions exhibit positive effects on delaying thermal runaway (see the SI for more detailed data). In addition, in Fig. 7d, the maximum temperature (T_{max}) of each cell in the thermal runaway process falls in the range between 600 and 800 ℃, showing neglibile differences between nitrogen and argon dilutions. This can be due to a closer contact among the battery bundles. However, it should be noted that the cost of argon is around three times of nitrogen. From the cost-performance viewpoint, it is recommended to use nitrogen as the dilution gas in battery-safety applications.

Fig. 7e and Fig. 7f illustrates the smoke flow direction after the experiments with two different inert dilution gases. During the experiments, the produced fire smoke is mixed well with continuous gas flow to maintain a dynamic pressure and atmosphere equilibrium. After the experiments, the smoke flow direction vary from each other with Ar gas and N_2 gas. For the N_2 dilution, the white smokes move upward near the ceiling, while in the argon dilution configuration, the smokes move downward near the floor (note that with continuous dilution gas inlet, most of the gas has been drawn out of the chamber). The major reason lies in the relative density of the dilution gas and the air (referring to Table 1). To be more specifically, the smoke particle will move along with the dilution gas. For those dilution inert gas with a similar density with the air (such as nitrogen in this study), the hotter smoke particle has a larger buoyancy drag that tends to move award. While for those inert gas with a much larger density than the air, the obvious density difference will exert a greater influence on flowing direction, that is they will move downward. This phenomenon can help guide the potential waste gas disposal. For example, for the storage warehouse using inert nitrogen dilution, the smoke emissions should be ventilated from the ceiling for further purification. Whereas for those using inert argon dilution, it is recommended to ventilate smoke at the lower area.

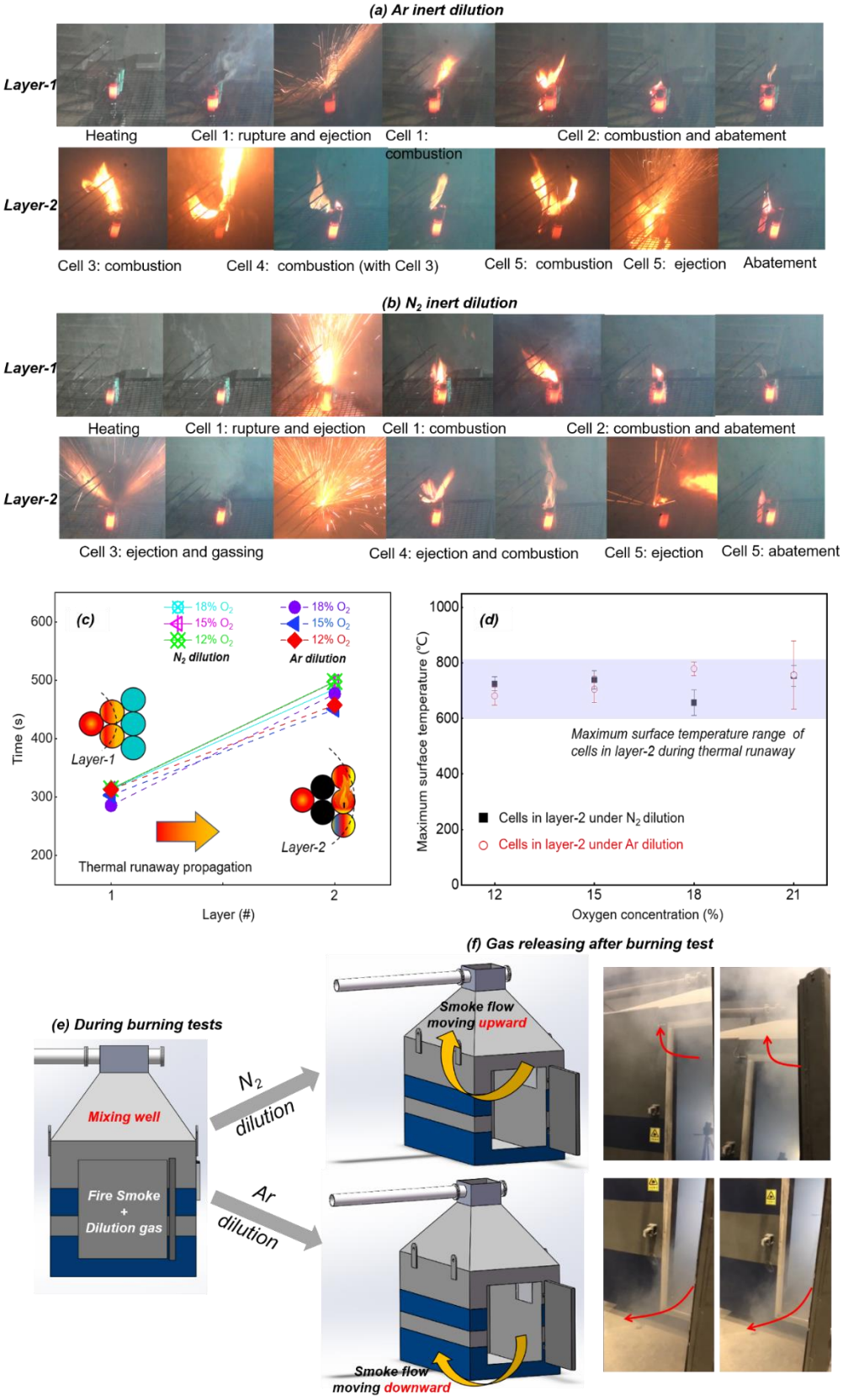

Fig. 7. (a-b) Fire behaviors of battery modules in different dilution gas (15 % O_2); (c) comparison on the $\overline{t_{L1}}$ and $\overline{t_{L2}}$ between nitrogen and argon dilutions; (d) the maximum temperature (T_{max}) for each cell in both dilution gases under different oxygen concentrations; and (e-f) schematic of smoke flow directions with different inert dilution gas.

4. Micro morphology analysis

X-Ray CT imaging

X-ray computed tomography (X-ray CT) is a non-destructive detecting technique to observe the internal structure change of materials [60]. Fig. 8 presents the X-ray CT images of (a) the fresh cell, (b) the burnt cells the 21% O_2 atmosphere and (c) the burnt cells the 15% O_2 atmosphere. Note that the pictures are colored to make it easier to distinguish some difference and the original pictures are provided in Fig. S3 in the SI. For the fresh cell in Fig. 8a, the winding structures of the positive and negative plates are in good order with an equal spacing among them (around 183.6 *um*). A blank area with a regular boundary is observed in the center part. However, for the burnt cells in Fig. 8b, the positive and negative plates appear disorganized. This is mostly possible due to the fast gas generation during the flaming and explosions of the cells after thermal abusing [59, 60]. The blank area in the center disappears owing to the structural failure. The spacing between the plates increases to around 507.8 *um*, and the arrangement of electronic plates seems loose.

Besides, some fine particles are observed among the plates. These are the molten drops of the metal aluminum, whose melting point is around 660 ºC. During the combustion of the cells, the metal aluminum melts, and part of it ejects with combustible gases through the safety valve. In contrast, the rest exists as droplets among the plates. Compared to the burnt cell in the air, more molten drops remaining among the plates can be observed in the burnt cell in the atmosphere with 15% O_2 in Fig. 8c. This can be attributed to the shorter flaming time and incomplete combustion in such an oxygen-lean environment, which produces less possibility for aluminum droplets to eject outside. In addition, the spacing among the plates is smaller (around 279.4 *um*) than the cell burnt in the air. These sample characterizations further confirm that the flaming combustion outside the cells is much less complete, and chemical reactions inside cells are also weaker in the oxygen-lean atmosphere with inert gas dilution.

Energy-dispersive X-Ray spectrometry analysis

The micromorphology figures were obtained using Energy-dispersive X-Ray spectrometry (EDS) coupled with field emission scanning electron microscopy (SEM). Fig. 8 presents the EDS mapping for negative electrode materials of both fresh and burnt cells. In Fig. 8(g) and (k), the elements of carbon (C), oxygen (O), and fluorine (F) can be distinguished in the negative electrode materials with different colors of C (red), O (light blue) and F (purple). Combined with the EDS spectrums in Fig. 8(f) and (j), it is found that in the fresh cell, C, O, and F account 82.56 ± 0.64 %, 8.49 ± 0.46 %, and 8.95 ± 0.52 % respectively. While in the burnt cell, C, O and F account 89.13 ± 0.65 %, 9.08 ± 0.53 % and 1.79 ± 0.41 % respectively. The significant decrease on the F element results from the consumption of the electrolyte (including lithium hexafluorophosphate) during the flaming combustion. Furthermore, with lower oxygen concentration, the F residue becomes more (Fig. S4). This confirms a less degree of burning behavior in the lower oxygen concentration.

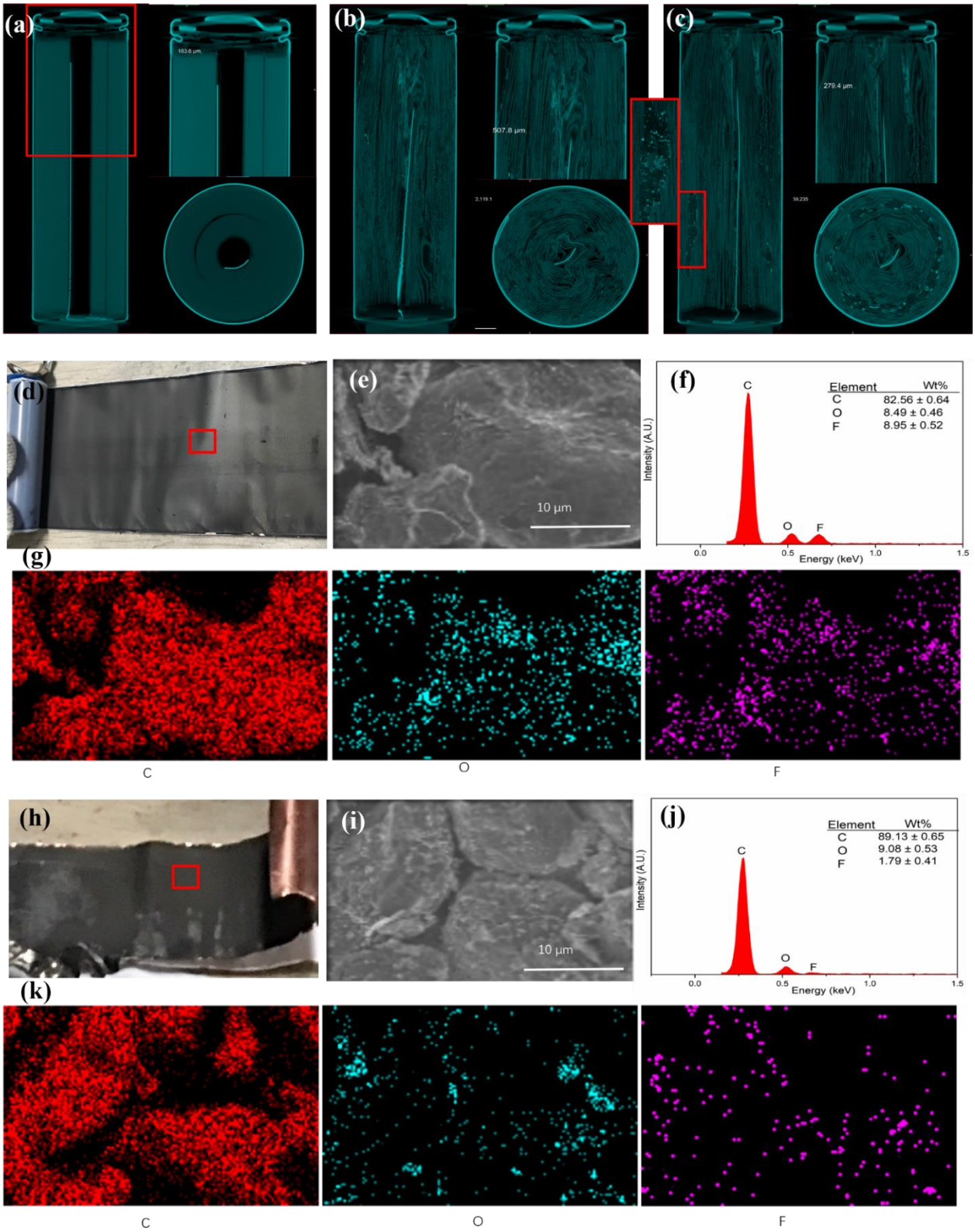

Fig. 8. X-ray CT images of (a) the fresh cells; (b) the burnt cells in the 21% O_2 atmosphere; (c) the burnt cells in the 15 % O_2 atmosphere and SEM-EDS analysis for negative electrode materials of both fresh and burnt cells: (d) & (h) photographs of internal structure; (e) & (i) SEM images for EDS; (f) & (j) EDS spectrums; (g) & (k) element mappings.

In addition, during the EDS analysis, it is found that the element of nitrogen (N) cannot be distinguished in the point map. This confirms that in the environment with oxygen, the lithium will first start a chemical reaction with oxygen rather than nitrogen; thus, there is little lithium nitride (LiN) existing in the combustion residue. Besides, a comparison of the samples of negative electrode materials of cells in environments with different oxygen concentrations is conducted (Fig. S3 in the SI). All burnt cells present less concentration of the element F, and the residues of element F on the burnt cells in the atmosphere with either nitrogen or argon exhibit extremely higher values than that in the air. This can be attributed to the less incomplete combustion process of the electrolyte in the atmosphere with inert dilution with less flame duration, as discussed above.

5 Conclusions

In this study, a series of experiments has been conducted on cylindrical Li-ion battery packs to investigate the effect of oxygen concentration (12-21%) and dilution gases (nitrogen and argon) on inhibiting the battery fire and thermal runaway propagation. The main conclusions of this study were drawn as follows:

(1) When the oxygen concentration is reduced from 21% to 12%, the thermal-runaway time for Layer 2 is delayed due to the weakened flame heating. The time interval (between Layers 1 and 2) increases from 136 s (21% O_2) to 196 s (12% O_2), indicating the rate of thermal-runaway propagation is reduced by 44%.

(2) The mass-loss ratios of the cells (excluding the heater) are 39.2%, 35.9%, 30.3%, and 30.0% at 21%, 18%, 15%, and 12% O_2, respectively. This further suggests that reducing the oxygen concentration also weakens the thermal-runaway processes of the battery cells.

(3) By comparing different inert gases, it is found that argon and nitrogen dilution can slow down the thermal runaway propagation over battery layers in a similar manner, so using nitrogen in the real applications is more cost-effective. Nevertheless, the ventilation method for different inert gases are also different.

(4) From the X-ray images, the a loose and messy internal structure is observed from the burnt cells with the electrolyte plate spacing increase from 183.6 *um* to 507.8 *um*. For the burnt cell in the hypoxic environment, more molten drops can be seen among the plates. EDS mapping reveals a dramatic reduction on the content of element F after combustion (8.95 ± 0.52 % vs. 1.79 ± 0.41 %), which increase with decreasing oxygen concentration. This confirms a lower degree of hazards in the lower oxygen concentration.

These outcomes provide new references and guidance in the application of inert dilution in the battery fire, storage and transportation. However, they were conducted on limited configurations in this experimental work. In the future, more researches will be conducted using different methodologies like simulation methodology can be considered with more environmentally-friendly solutions.

Acknowledgements

This work was sponsored by the National Natural Science Foundation of China (No. 51991352) and the Research Grants Council of the Hong Kong Special Administrative Region (CityU 11208617). This work was carried out at Facilities of the State Key Laboratory of Fire Science (SKLFS), USTC. The authors thank Dr. Dechuang Zhou for his contribution in the maintenance of the hypoxic and low-pressure conditions and establishing special experimental environment systems.

References

[1] Tran M K, Bhatti A, Vrolyk R, et al. A Review of Range Extenders in Battery Electric Vehicles: Current Progress and Future Perspectives[J]. World Electric Vehicle Journal, 2021, 12(2): 54.

[2] Panchal S, Mathew M, Fraser R, et al. Electrochemical thermal modeling and experimental measurements of 18650 cylindrical lithium-ion battery during discharge cycle for an EV[J]. Applied Thermal Engineering, 2018, 135: 123-132.

[3] Yan W, Wang Z, Chen S. Quantitative analysis on the heat transfer modes in the process of thermal runaway propagation in lithium-ion battery pack under confined and semi-confined space[J]. International Journal of Heat and Mass Transfer, 2021, 176: 121483.

[4] Akhoundzadeh M H, Panchal S, Samadani E, et al. Investigation and simulation of electric train utilizing hydrogen fuel cell and lithium-ion battery[J]. Sustainable Energy Technologies and Assessments, 2021, 46: 101234.

[5] Xiao C, Zhang G, Li Z, et al. Custom design of solid–solid phase change material with ultra-high thermal stability for battery thermal management[J]. Journal of Materials Chemistry A, 2020, 8(29): 14624-14633.

[6] Finegan D P, Darst J, Walker W, et al. Modelling and experiments to identify high-risk failure scenarios for testing the safety of lithium-ion cells[J]. Journal of Power Sources, 2019, 417: 29-41.

[7] Lai X, Huang Y, Deng C, et al. Sorting, regrouping, and echelon utilization of the large-scale retired lithium batteries: A critical review[J]. Renewable and Sustainable Energy Reviews, 2021, 146: 111162.

[8] Lai X, Wang S, Wang H, et al. Investigation of thermal runaway propagation characteristics of lithium-ion battery modules under different trigger modes[J]. International Journal of Heat and Mass Transfer, 2021, 171: 121080.

[9] Baird A R, Archibald E J, Marr K C, et al. Explosion hazards from lithium-ion battery vent gas[J]. Journal of Power Sources, 2020, 446: 227257.

[10] Kong D, Wang G, Ping P, et al. Numerical investigation of thermal runaway behavior of lithium-ion batteries with different battery materials and heating conditions[J]. Applied Thermal Engineering, 2021, 189: 116661.

[11] Li X, Huang Q, Deng J, et al. Evaluation of lithium battery thermal management using sealant made of boron nitride and silicone[J]. Journal of Power Sources, 2020, 451: 227820.

[12] Huang Z, Li H, Mei W, et al. Thermal runaway behavior of lithium iron phosphate battery during penetration[J]. Fire technology, 2020: 1-22.

[13] Li W, Rao S, Xiao Y, et al. Fire boundaries of lithium-ion cell eruption gases caused by thermal runaway[J]. Iscience, 2021, 24(5): 102401.

[14] Mevawalla A, Panchal S, Tran M K, et al. One dimensional fast computational partial differential model for heat transfer in lithium-ion batteries[J]. Journal of Energy Storage, 2021, 37: 102471.

[15] Chen H, Buston J E H, Gill J, et al. An experimental study on thermal runaway characteristics of lithium-ion batteries with high specific energy and prediction of heat release rate[J]. Journal of Power Sources, 2020, 472: 228585.

[16] Li Y, Han X, Feng X, et al. Errors in the reference electrode measurements in real lithium-ion batteries[J]. Journal of Power Sources, 2021, 481: 228933.

[17] Sun T, Xu B, Cui Y, et al. A sequential capacity estimation for the lithium-ion batteries combining incremental capacity curve and discrete Arrhenius fading model[J]. Journal of Power Sources, 2021, 484: 229248.

[18] Li S, Li K, Xiao E, et al. Real-time peak power prediction for zinc nickel single flow batteries[J]. Journal of Power Sources, 2020, 448: 227346.

[19] Weng J, He Y, Ouyang D, et al. Honeycomb-inspired design of a thermal management module and its mitigation effect on thermal runaway propagation[J]. Applied Thermal Engineering, 2021: 117147.

[20] Ping P, Kong D, Zhang J, et al. Characterization of behaviour and hazards of fire and deflagration for high-energy Li-ion cells by over-heating[J]. Journal of Power Sources, 2018, 398: 55-66.

[21] Jin C, Sun Y, Wang H, et al. Model and experiments to investigate thermal runaway characterization of lithium-ion batteries induced by external heating method[J]. Journal of Power Sources, 2021, 504: 230065.

[22] Kim J, Mallarapu A, Finegan D P, et al. Modeling cell venting and gas-phase reactions in 18650 lithium ion batteries during thermal runaway[J]. Journal of Power Sources, 2021, 489: 229496.

[23] Abada S, Petit M, Lecocq A, et al. Combined experimental and modeling approaches of the thermal runaway of fresh and aged lithium-ion batteries[J]. Journal of Power Sources, 2018, 399: 264-273.

[24] Wang L, Duan X, Liu B, et al. Deformation and failure behaviors of anode in lithium-ion batteries: Model and mechanism[J]. Journal of Power Sources, 2020, 448: 227468.

[25] Wang W, Li Y, Cheng L, et al. Safety performance and failure prediction model of cylindrical lithium-ion battery[J]. Journal of Power Sources, 2020, 451: 227755.

[26] Said A O, Lee C, Stoliarov S I, et al. Comprehensive analysis of dynamics and hazards associated with cascading failure in 18650 lithium ion cell arrays[J]. Applied Energy, 2019, 248: 415-428.

[27] Baird A R, Archibald E J, Marr K C, et al. Explosion hazards from lithium-ion battery vent gas[J]. Journal of Power Sources, 2020, 446: 227257.

[28] Chen S, Wang Z, Yan W. Identification and characteristic analysis of powder ejected from a lithium ion battery during thermal runaway at elevated temperatures[J]. Journal of hazardous materials, 2020, 400: 123169.

[29] Mattinen U, Klett M, Lindbergh G, et al. Gas evolution in commercial Li-ion battery cells measured by on-line mass spectrometry–Effects of C-rate and cell voltage[J]. Journal of Power Sources, 2020, 477:

228968.

[30] Larsson F, Anderson J, Andersson P, et al. Thermal modelling of cell-to-cell fire propagation and cascading thermal runaway failure effects for lithium-ion battery cells and modules using fire walls[J]. Journal of the electrochemical society, 2016, 163(14): A2854.

[31] Shack P, Iannello C, Rickman S, et al. NASA Perspective and Modeling of Thermal Runaway Propagation Mitigation in Aerospace Batteries[C]//NASA Aerospace Battery Workshop. 2014: 18-20.

[32] Feng X, Ren D, He X, et al. Mitigating thermal runaway of lithium-ion batteries[J]. Joule, 2020, 4(4): 743-770.

[33] Chombo P V, Laoonual Y. A review of safety strategies of a Li-ion battery[J]. Journal of Power Sources, 2020, 478: 228649.

[34] Xia G, Cao L, Bi G. A review on battery thermal management in electric vehicle application[J]. Journal of power sources, 2017, 367: 90-105.

[35] Wilke S, Schweitzer B, Khateeb S, et al. Preventing thermal runaway propagation in lithium ion battery packs using a phase change composite material: an experimental study[J]. Journal of Power Sources, 2017, 340: 51-59.

[36] Li Q, Yang C, Santhanagopalan S, et al. Numerical investigation of thermal runaway mitigation through a passive thermal management system[J]. Journal of Power Sources, 2019, 429: 80-88.

[37] Weng J, Ouyang D, Yang X, et al. Alleviation of thermal runaway propagation in thermal management modules using aerogel felt coupled with flame-retarded phase change material[J]. Energy Conversion and Management, 2019, 200: 112071.

[38] Zhang J, Li X, Zhang G, et al. Experimental investigation of the flame retardant and form-stable composite phase change materials for a power battery thermal management system[J]. Journal of Power Sources, 2020, 480: 229116.

[39] Said A O, Lee C, Stoliarov S I. Experimental investigation of cascading failure in 18650 lithium ion cell arrays: impact of cathode chemistry[J]. Journal of Power Sources, 2020, 446: 227347.

[40] Liu X, Stoliarov S I, Denlinger M, et al. Comprehensive calorimetry of the thermally-induced failure of a lithium ion battery[J]. Journal of Power Sources, 2015, 280: 516-525.

[41] Liu X, Wu Z, Stoliarov S I, et al. Heat release during thermally-induced failure of a lithium ion battery: Impact of cathode composition[J]. Fire Safety Journal, 2016, 85: 10-22.

[42] Natarajan J, Lieuwen T, Seitzman J. Laminar flame speeds of H2/CO mixtures: Effect of CO2 dilution, preheat temperature, and pressure[J]. Combustion and flame, 2007, 151(1-2): 104-119.

[43] Prathap C, Ray A, Ravi M R. Investigation of nitrogen dilution effects on the laminar burning velocity and flame stability of syngas fuel at atmospheric condition[J]. Combustion and Flame, 2008, 155(1-2): 145-160.

[44] Li S, Zhang Y, Qiu X, et al. Effects of inert dilution and preheating temperature on lean flammability limit of syngas[J]. Energy & fuels, 2014, 28(5): 3442-3452.

[45] Kim C H, Kwon O C, Faeth G M. Effects of halons and halon replacements on hydrogen-fueled laminar premixed flames[J]. Journal of propulsion and power, 2002, 18(5): 1059-1067.

[46] Wang Z, Zuo H, Liu Z, et al. Impact of N2 dilution on combustion and emissions in a spark ignition CNG engine[J]. Energy conversion and management, 2014, 85: 354-360.

[47] Y. Zhang, W. Shen, H. Zhang, Y. Wu, J. Lu, Effects of inert dilution on the propagation and extinction of lean premixed syngas/air flames, Fuel. 157 (2015) 115–121.

[48] N.M. Hafiz, M.R.A. Mansor, W.M.F. Wan Mahmood, Simulation of the combustion process for a CI hydrogen engine in an argon-oxygen atmosphere, International Journal of Hydrogen Energy. 43 (2018) 11286–11297.

[49] Qi S, Du Y, Zhang P, et al. Effects of concentration, temperature, humidity, and nitrogen inert dilution on the gasoline vapor explosion[J]. Journal of hazardous materials, 2017, 323: 593-601.

[50] Baird A R, Archibald E J, Marr K C, et al. Explosion hazards from lithium-ion battery vent gas[J]. Journal of Power Sources, 2020, 446: 227257.

[51] Huang P, Ping P, Li K, et al. Experimental and modeling analysis of thermal runaway propagation over the large format energy storage battery module with Li4Ti5O12 anode[J]. Applied energy, 2016, 183: 659-673.

[52] D. Ren, X. Feng, L. Liu, H. Hsu, L. Lu, L. Wang, X. He, M. Ouyang, Investigating the relationship between internal short circuit and thermal runaway of lithium-ion batteries under thermal abuse condition, Energy Storage Materials. 34 (2021) 563–573.

[53] Weng J, Yang X, Ouyang D, et al. Comparative study on the transversal/lengthwise thermal failure propagation and heating position effect of lithium-ion batteries[J]. Applied Energy, 2019, 255: 113761.

[54] Liu Y, Sun P, Lin S, et al. Self-heating ignition of open-circuit cylindrical Li-ion battery pile: Towards fire-safe storage and transport[J]. Journal of Energy Storage, 2020, 32: 101842.

[55] He X, Restuccia F, Zhang Y, et al. Experimental study of self-heating ignition of lithium-ion batteries during storage: effect of the number of cells[J]. Fire technology, 2020, 56(6): 2649-2669.

[56] Gao S, Lu L, Ouyang M, et al. Experimental study on module-to-module thermal runaway-propagation in a battery pack[J]. Journal of the electrochemical society, 2019, 166(10): A2065.

[57] Chen M, Liu J, He Y, et al. Study of the fire hazards of lithium-ion batteries at different pressures[J]. Applied Thermal Engineering, 2017, 125: 1061-1074.

[58] Link S, Huang X, Fernandez-Pello C, et al. The effect of gravity on flame spread over PMMA cylinders[J]. Scientific reports, 2018, 8(1): 1-9.

[59] Fu Y, Lu S, Shi L, et al. Ignition and combustion characteristics of lithium ion batteries under low atmospheric pressure[J]. Energy, 2018, 161: 38-45.

[60] Xie S, Ren L, Yang X, et al. Influence of cycling aging and ambient pressure on the thermal safety features of lithium-ion battery[J]. Journal of Power Sources, 2020, 448: 227425.